RSC Advances

ROYAL SOCIETY OF CHEMISTRY

www.rsc.org/advances

RSC Advance

RSCPublishing

PAPER

Template-synthesis of carbon self-doped g-C_3N_4 with enhanced visible to near-infrared absorption and photocatalytic performance

Received (in XXX, XXX) Xth XXXXXXXXX 20XX,

Accepted Xth XXXXXXXXX 20XX

Zaiwang Zhao[a], Yanjuan Sun[a], Fan Dong[a,*], Yuxin Zhang[b,c*], Han Zhao[d]

DOI: 10.1039/b000000x

www.rsc.org/nanoscale

In order to fully address the low surface area, fast charge recombination and limited visible light absorption of pristine g-C_3N_4, we presented a novel straightforward strategy toward synthesis of carbon self-doped g-C_3N_4 by using porous carbon foam as a soft-template. The C-doped g-C_3N_4 displayed high BET surface area (65 m^2/g), extended absorption from visible light up to near-infrared range (800 nm) and accelerated electrons-holes separation. The role of carbon doping on the band structure and electrical conductivity was revealed. The optimized C-doped g-C_3N_4 demonstrated exceptional high photocatalytic performance toward purification of NO in air, which exceeded other reported visible-light photocatalysts, such as nonmetal-doped TiO_2, BiOBr, $(BiO)_2CO_3$ and porous g-C_3N_4. This decent C-doped g-C_3N_4 photocatalysts also showed good photocatalytic stability in NO removal. The present work could provide some new insights into the modification and understanding of semiconductor photocatalyst with self-doping.

1. Introduction

Contriving efficient visible-light-driven (VLD) photocatalysts has extensively provoked great attentions in materials chemistry.[1-15] Different types of photocatalysts are utilized in photocatalytic domains, including the metal-containing photocatalyst (TiO_2, $AgPO_4$, Bi_2WO_6),[3-6] metal-free photocatalyst (g-C_3N_4, S, P),[7-18] SPR-mediated noble metal photocatalysts (Au, Ag)[19-23] and non-noble metal photocatalyst (Bi, Cu).[24-26] Especially, g-C_3N_4 as earth-abundant, economically available and robust photocatalyst has demonstrated great potential and attracted increasing interests.[13-15] Nevertheless, the pristine g-C_3N_4 has low surface area, fast charge recombination and can only utilize blue light up to 450 nm, which limits the large-scale application.

Various strategies have been adopted to enhance the photocatalytic capability of g-C_3N_4.[2,13,14,27] Among these strategies, doping is considered as an effective way. For instance, boron-doped could improve the photocatalytic performance of g-C_3N_4 in methyl orange photodegradation owing to increased light absorption of the catalyst and promote the electrical conductivity of g-C_3N_4.[28] Sulfur-doping could enhance the photoreactivity of g-C_3N_4 owing to the co-contribution of enlarged BET surface areas and promoted light absorption.[2] However, the anion doping strategy is also likely to have some detrimental shortcomings such as poor oxidation power of the photo-excited hole and fast recombination of photo-generated electrons/holes pairs due to the impurity as the defects induced by doping asymmetry.[29]

To date, it has been demonstrated that self-doping not only could fine-tune the surface architectures and electronic properties of semiconductor photocatalysts, but also avoid the introduction of foreign impurity and defects which may act as the recombination centers.[30-34] For example, Jiang et al. successfully fabricated self-doping BiOCl with remarkable visible light driven photocatalytic activity.[33] Yu and his colleagues designed nitrogen self-doped nanosized TiO_2 sheets with extremely high visible-light photocatalytic performance in hydrogen production.[34] Moreover, self-doping method have also been successfully reported in the g-C_3N_4 systems with excellent photocatalytic activity.[27,35] Zhang and et al. firstly investigated carbon self-doped g-C_3N_4 theoretically and experimentally, and demonstrated that this carbon self-doped strategy can increase visible-light absorption and electrical conductivity as well as surface area resulting in enhancing photoxidation capability.[27] These successes further demonstrated that carbon self-doping was indeed an effective and potential method to advance the photoxidation ability of g-C_3N_4. However, the mechanism of carbon self-doped g-C_3N_4 is still unclear and the application of carbon-doped g-C_3N_4 in air purification has not been reported so far.

Herein, we introduced an *in situ* one-pot strategy to prepare the carbon self-doped g-C_3N_4 by using commercially available polyporous carbon foam as a template. We also investigated the influence of the mass ratio of the precursors of melamine and the carbon foam. To evaluate the photocatalytic performance, all the as-prepared carbon self-doped g-C_3N_4 samples were applied to the photocatalytic removal of NO in air under visible light irradiation. The optimized sample demonstrated an excellent visible-light photocatalytic capability, which was ascribed to the enlarged BET surface area, the hindered photo-exited carriers recombination as well as the enhanced the light absorption from visible light to near-infrared range.

2. Experimental Section

2.1 Catalysts Preparation.

All the reagents employed in this study were of analytical grade and used without further purification. In a typical synthesis, melamine powder of different masses (2.0, 5.0 and 8.0 g) were put into three different alumina crucibles (50ml), respectively. Then 20 mL deionized water was added into the alumina crucibles, and heated and stirred to make complete dissolusion. Afterwards, 0.3 g melamine porous resin foam (MRF, supplied by Puyang Green Universh Chemical Co., Ltd.) was cut into small pieces and then added to the solution above, respectively. After recrystallized in 100 ^{o}C, the alumina crucibles was placed in a muffle furnace, and treated at 550 ^{o}C for 2 h with a heating rate of 15 ^{o}C/min. After the reaction, the alumina crucible was cooled to room temperature. The resultant g-C_3N_4 were collected and ground into powders. The different g-C_3N_4 samples prepared from different precursor masses (2, 5 and 8 g) with MRF were labeled as 2M-CF, 5T-CF and 8M-CF, respectively. Pure g-C_3N_4 as a reference was also prepared by directly pyrolysis of 5 g melamine without adding MRF, and labeled as 5M.

2.2 Characterization.

The X-ray diffraction (XRD) patterns of the samples were obtained using an X-ray diffractometer equipped with intense Cu Kα radiation (Model D/max RA, Rigaku Co., Japan). Carbon to nitrogen ratio (C/N) of the photocatalysts was detected by elemental analysis (EA, Vario ELIII CHNSO). The morphology, structure and chemical composition of the obtained products were analyzed using scanning electron microscope (SEM, JEOL model JSM-6490, Japan), transmission electron microscope (TEM, JEM-2010, Japan). The Brunauer–Emmett–Teller (BET) specific surface area (S_{BET}) of the samples were determined using a nitrogen adsorption apparatus (ASAP 2020, USA) with all samples degassed at 100 ℃ for 12 h prior to measurements. X-ray photoelectron spectroscopy (XPS) measurement was carried out to investigate the surface chemical compositions and states with Al Kα X-ray ($h\nu$ = 1486.6 eV) radiation source operated at 150 W (Thermo ESCALAB 250, USA). The UV-vis diffuse reflection spectra (UV-vis DRS) were obtained for the dry-pressed disk samples by using a Scan UV-vis spectrophotometer (UV-2450, Shimadzu, Japan) with 100% $BaSO_4$ as the standard sample. Photoluminescence (PL, F-7000, HITACHI, Japan) was used to investigate the optical properties of the obtained samples.

2.3 Evaluation of Photocatalytic Performance.

The photocatalytic capability of the as-synthesized samples was evaluated by removing NO at ppb level in a continuous flow reactor (Scheme 1). The reactor was 4.5 L (30 cm × 15 cm × 10 cm), made of polymeric glass, and covered with Saint-Glass. A commercial tungsten halogen lamp (100 W) was vertically placed 20 cm above the reactor. A UV cut-off filter (420 nm) was applied to remove UV light for the test of visible light photocatalytic activity. The as-prepared sample (0.20 g) was dispersed in distilled water (50 ml) in a beaker via ultrasonic treatment for 10 min and then coated onto two glass dishes (12.0 cm in diameter). The coated dishes were pretreated at 70 ℃ to remove water in the suspension and placed at the centre of the reactor after cooling down to room temperature. The NO gas was acquired from a compressed gas cylinder at a concentration of 100 ppm of NO (N_2 balance). The initial concentration of NO was diluted to about 600 ppb via air streaming. The flow rates of the air stream and NO were controlled at 2.4 L min^{-1} and 15 mL min^{-1}, respectively. The two gas streams were then premixed in a three-way valve. The relative humidity is controlled at 50% in the air stream. When the adsorption-desorption equilibrium was achieved, the lamp was turned on. The concentration of NO was measured every one min by using a NO_x analyzer (Thermo Scientific, 42i-TL), which also monitored the concentration of NO_2 and NO_x (NO_x represents NO + NO_2). The removal ratio (η) of NO was calculated using η (%) = $(1 - C/C_0) \times 100\%$, where C is the outlet concentration of NO after reaction for time t, and C_0 represents the inlet concentration after achieving adsorption-desorption equilibrium. The kinetics of photocatalytic NO removal reaction is a pseudo-first-order reaction at low NO concentration as $\ln(C_0/C) = k_{app}t$, where k_{app} is the apparent rate constant.

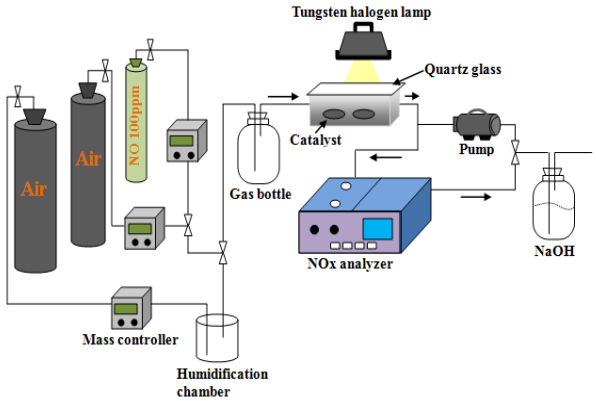

Scheme 1. The diagrams of experimental setup for NO removal.

3. Results and Discussion

3.1 Phase Structures and Chemical Constitutions

Two typical diffraction peaks ascribed to g-C_3N_4 (JCPDS 87-1526) were detected (Fig. 1) both in g-C_3N_4 and carbon self-doped g-C_3N_4 samples, demonstrating that carbon self-doping do not change the architectures of the g-C_3N_4. The stronger peak centered at 27.1 ° was ascribed to the (002) diffraction peak reflecting the interplanar graphitic stacking and the minor peak at around 13.1 ℃an be indexed as the (100) diffraction peak in accordance of the in-plane tri-s-triazine units.[15] Elemental analysis was further performed to test the molar ratio of carbon to nitrogen (C/N) both in the pure and C-doped g-C_3N_4. The C/N value of g-C_3N_4 is 0.561, while a slight enhancement of C/N value 0.563, 0.571 and 0.590 for C-doped 8M-CF, 5M-CF and 2M-CF can be observed. The gradually increased C/N ratio revealed that the carbon has been successfully incorporated into g-C_3N_4. Besides, this phenomenon of progressively improved carbon contents of g-C_3N_4 was also obtained (the C/N value 0.751 for g-C_3N_4 and 0.766 for C-doped g-C_3N_4), reported by other groups.[27]

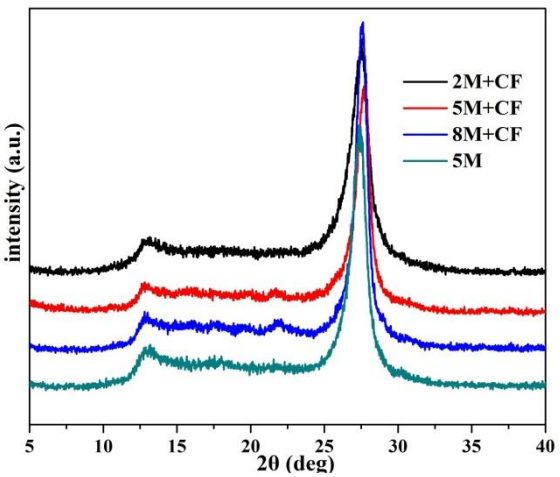

Fig. 1 XRD patterns of the pure and C-doped g-C_3N_4

FT-IR spectra is utilized to confirm the molecular structure of all samples. As shown in Fig. 2, the strong absorption peak around 700-800 cm^{-1} region can be observed, which is assigned to the bending vibration mode of CN heterocycles, while peak centered at 810 cm^{-1} is the characteristic plane bending vibration mode of the triazine units (Fig. 2a).[36] The peak observed at 1200-1600 cm^{-1} is mainly due to stretching mode of C-N heterocycles, and the broad bands in the region 3000-3700 cm^{-1} (Fig. 2b) are assigned to the adsorbed H_2O molecules and N-H vibration.[37]

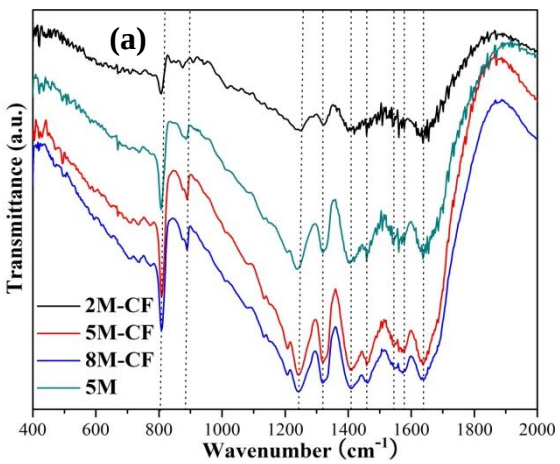

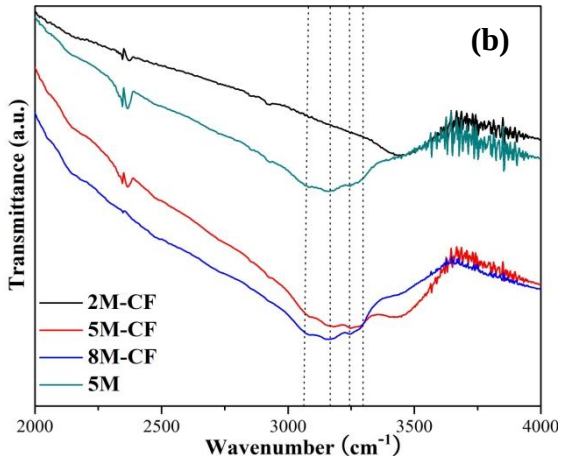

Fig. 2 FT-IR spectra of the pure and C-doped g-C_3N_4 in the range of 400-2000 cm^{-1} (a) and 2000-4000 cm^{-1} (b).

The XPS was further carried out to determine the chemical composition of the pure g-C_3N_4 and C-doped g-C_3N_4. As shown in Fig. 3a, the XPS spectra of C 1s of the 5M and 5M-CF samples can be corresponded to two typical peaks centered at binding energies of 284.7 and 288.2 eV, which are characteristic of the C–N–C coordination and C–C bonds, respectively.[29, 38] The area ratios of the two typical peaks at 284.6 and 288.2 eV were calculated to be 0.095 and 0.132 for 5M and 5M-CF, respectively. Furthermore, three peaks ascribing to N1s of the two samples also can be observed (Fig. 3b). The major peaks centered at 400.6 and 398.4 eV can be indexed to the N–C_3 and C–N–C groups[29] with peak area ratios of 0.183 and 0.170 for g-C_3N_4 and carbon self-doped g-C_3N_4. These consequence as well as the shift of the main C and N peaks reflected that the bridging N was replaced by C elements because of the self-doped carbon (Fig. 3c and 3d).[29] Zhang's group have reported that a delocalized big π bonds will be formed among the substituted carbons and the hexatomic rings when the bridging N atoms was replaced by C atoms,[29] which would enhance electrical conductivity of g-C_3N_4. The delocalized π bonds are favorable for the electrons movement and transfer, resulting in impeding photoexcited electrons-holes recombination.[29, 38] The present result is consistent with previous report.[29, 38] The concentration of the C dopant was estimated to be 7 % on the basis of XPS result.

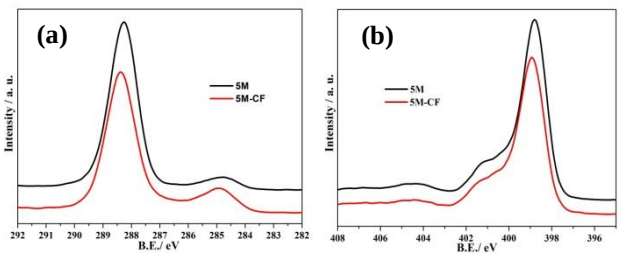

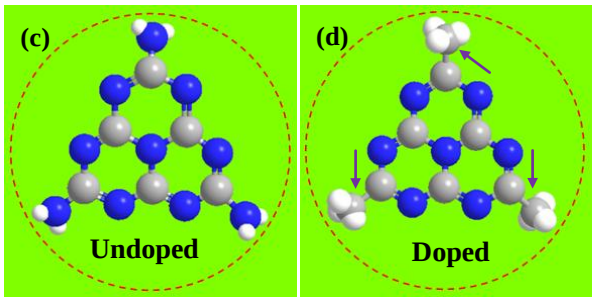

Fig 3. XPS spectra of 5M and 5M-CF samples, C1s (a), N1s (b); and crystal structures of g-C_3N_4 (c) and C-doped g-C_3N_4(d); the gray, blue and white balls represent the carbon, nitrogen, hydrogen atoms.

3.2 Morphology and Mesoporous structure

The carbon self-doping strategy not only can tune the electrons architectures, but also exert significant influence on the microstructures. Fig. 4 shows the morphology of the as-synthesized g-C_3N_4 and carbon-doped g-C_3N_4. As can be seen, the pure 5M samples showed the aggregated morphologies with irregular layers (Fig. 4a and 4b). After introducing the carbon foam as a soft template, the sample is transformed to smaller, and numerous near-spherical nanoparticles when the mass ratio of the carbon foams and g-C_3N_4 is increased. The decreased size of the g-C_3N_4 layers is ascribed to the severance of the large layers, which is caused by the replaced bridging N atoms in corresponding to the XPS results. The TEM and high magnification TEM results (Fig. 5) also demonstrates the irregular morphology of g-C_3N_4 layers. The porous architecture is proved by N_2 adsorption–desorption isotherms and BJH characterizations (Fig. 6a and 6b). The BET surface areas are measured to be 11, 17, 65, 14 m^2g^{-1} for 5M, 2M-CF, 5M-CF and 8M-CF, respectively (Table 1). A mesoporous architecture with a pore size distribution centered at 3.5 nm can be observed for all samples, while in particular, a wide pore size distribution ranging from 3 to 50 nm for 5M-CF can be found. The enhanced BET surface can provide more active sites for absorptions and the mesoporous structures are beneficial for the reactants transference, resulting in high photocatalytic performance.

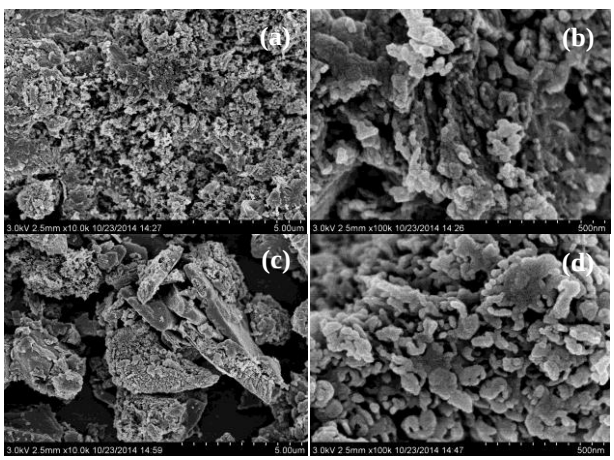

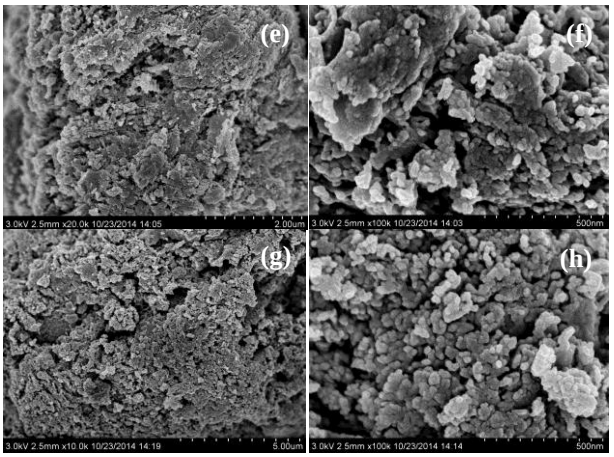

Fig. 4 SEM and magnifying view of pattern of 5M (a,b), 2M-CF (c,d), 5M-CF (e,f) and 8M-CF (g,h).

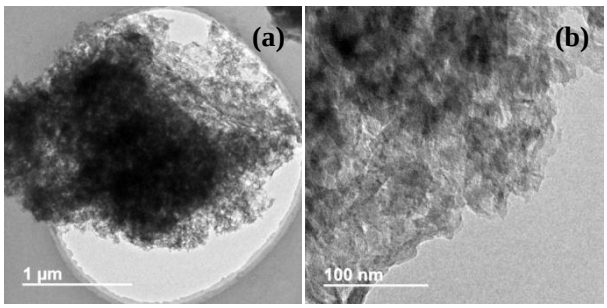

Fig. 5 TEM (a) and high magnification TEM (b) of 5M-CF

Table 1. The S_{BET}, pore volume, Peak diameter, band gap value and NO removal ratio of 2M-CF, 5M-CF, 8M-CF and 5M.

Sample name	S_{BET} (m^2/g)	Pore volume (cm^3/g)	Peak diameter (nm)	Band gap (eV)	NO η (%)
5M	11	0.080	22.4/30.3	2.62	14.3
2M-CF	17	0.082	12.7/19.1	1.87	8.1
5M-CF	65	0.293	13.9/18.0	2.05	50.1
8M-CF	14	0.085	14.4/24.2	2.24	22.3

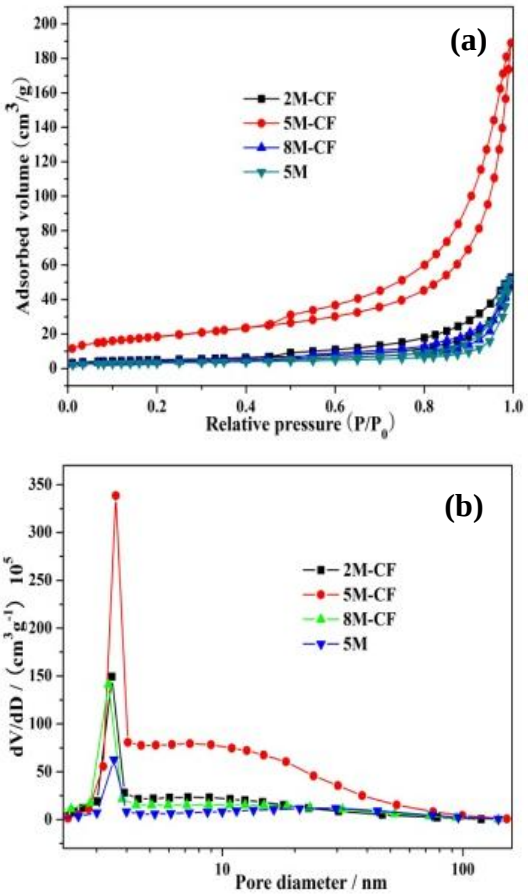

Fig. 6 N_2 adsorption-desorption isotherms of 5M, 2M-CF, 5M-CF, 8M-CF (a) and the corresponding pore-size distribution curves (b).

3.3 Optical Absorption and Band Structure

DRS UV-Vis absorption spectra (Fig. 7) of the as-synthesized photocatalysts in the wavelength range of 300–800 nm are recorded. As can be seen in Fig. 7a, the absorption edge of pure g-C_3N_4 is at 470 nm, which coincides with the previous literatures.[15] After carbon doping, the absorption is largely enhanced ranging from UV light to near-infrared light. Furthermore, the light absorption intensity is increased with increasing carbon doping contents. The light absorption response is consistent with the color variations of the samples (inserted in Fig. 7a). The band gaps are 2.62, 2.24, 2.05 and 1.87 eV for 5M, 8M-CF, 5M-CF and 2M-CF respectively, which are estimated by the plots of $(\alpha h\nu)^{1/2}$ versus photon energy of the samples(Fig. 7b). This diminished band gap can be ascribed to the negative shift of the valence band position (Fig. 7c), compared with that of the pristine g-C_3N_4, which are detected by the valence band XPS (+1.57 eV for 5M, while +1.23 eV for 5M-CF). These decreased band gap induced by the carbon self-doping strategy can effectively enlarge the light absorption ranges as well as strengthen the light absorption ability, which is expected to enhance the photocatalytic performance.

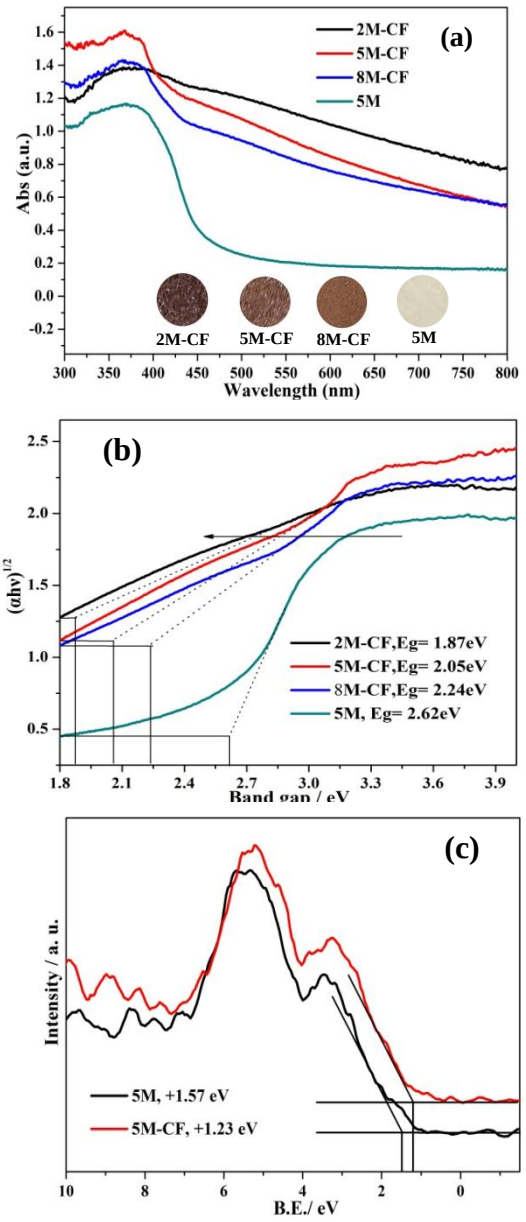

Fig. 7 UV–Vis DRS (a) and plots of $(\alpha h\nu)^{1/2}$ versus photon energy (b) of 5M, 2M-CF, 5M-CF, 8M-CF; (c) the valence band XPS the 5M and 5M-CF samples.

3.4 Charge Separation

Generally, there could be two fates for the photo-driven electron-hole pairs after photoexcitation. The first one is to transfer to the active sides of the surface of a photocatalyst for the subsequent chemical reactions. And the other is to recombine with each other without further reactions. The photoluminescence (PL) spectra of the samples were used to investigate the fates of the photoexcited electrons and holes under the 330 nm excitation at room temperature (Fig. 8). The results reflect that the pure g-C_3N_4

exhibits high electrons and holes recombination intensity, while the recombination rate is sharply hampered after carbon doping. The distinct suppression of recombination of the photo-induced electron-holes pairs is mainly assigned to the increased electrical conductivity of g-C_3N_4 induced by carbon self-doping because of the formation of delocalized big π bonds.[27] Furthermore, Zhang's group also has theoretically and experimentally demonstrated that carbon self-doping could enhance the electrical conductivity of g-g-C_3N_4 duo to the construction of delocalized big π bonds.[27] In general, low photo-driven electrons and holes recombination could result in high photocatalytic capability owing to the more generated active species which is a crucial factor in subsequent photocatalytic reactions.

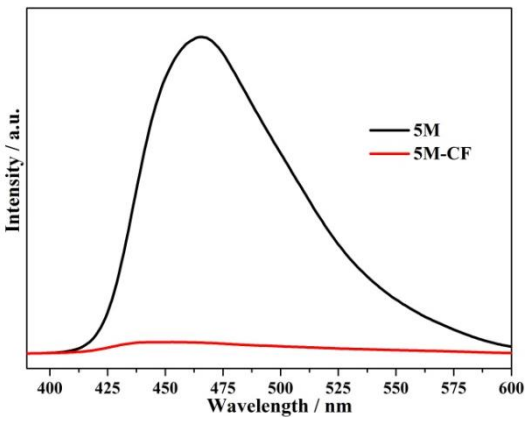

Fig. 8 Room temperature PL spectra (Excitation light source: 330 nm) of 5M-CF and 5M.

3.5 Electrical Conductivity Property

The enhanced electrical conductivity of the C-doping g-C_3N_4 was demonstrated by the electrochemical impedance spectroscopy (EIS) measurement (Fig. 9). This reduced arc radical reflects that proper carbon self-doping can highly enhance the electrical conductivity of g-C_3N_4 due to the formation of delocalized big π bonds induced by homogeneous substitution of bridging N atoms with C atoms.[27]

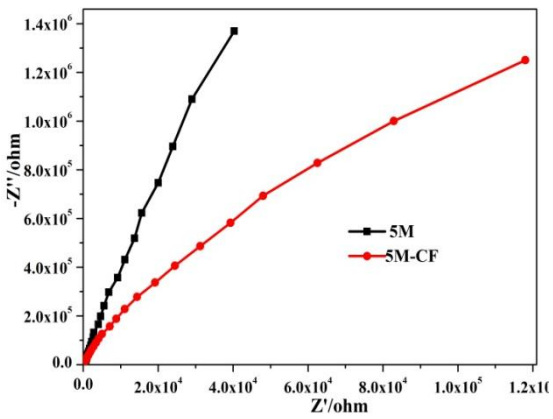

Fig. 9 Nyquist plots for 5M-CF and 5M samples electrodes under visible light irradiation (λ> 420 nm, [Na_2SO_4]=0.5 M).

3.6 Photocatalytic Properties

We first investigated the photocatalytic activity (Fig. 10) of the as-prepared samples in gas phase NO purification (ppb level) in a continuous reactor under visible-light illumination. Previous documents have proved that NO is stable and cannot be photo-oxidized under light illumination without photocatalysts, or in the presence of photocatalytic materials without light irradiation.[15] NO can be transformed to HNO_3 as the final product because of the photoxidation driven by the photo-generated reactive radicals of the photocatalysts under light irradiation.[14] For pure g-C_3N_4 (Fig. 10a), the photocatalytic performance for the NO removal ratio is about 14.3% when reaching an equilibrium in 30 min irradiation. The photocatalytic activities of C-doped g-C_3N_4 are 22.3, 50.1 and 8.1% for 8M-CF, 5M-CF and 2M-CF, respectively. Notably, the photodegradation ability of the optimized carbon-doped 5M-CF is increased to 50.1%, and even outperforms that of BiOBr (21.3%),[39] C-doped TiO_2 (21.8%),[40] N-TiO_2 (36.5%),[40] $(BiO)_2CO_3$ (43.5%)[41] and porous g-C_3N_4 (32.7%).[42] To further comprehend the reaction kinetics of the NO degradation catalyzed by pure and C-doped g-C_3N_4 samples, the experimental data were fitted by a first-order model (Fig. 10b).[43] The photodegradation constants were calculated to be 0.95 min^{-1} for 5M-CF, which is 3.8 times than that of 5M. The increased photocatalytic performance of the 5M-CF is the co-contributions of following factors: (1) the improved S_{BET} surface area provides more active sites for NO absorption, and (2) the enhanced light absorption ability from visible to near-infrared range which can induce more active species for photoxidation reaction; (3) last but significantly, the enhanced electrical conductivity of g-C_3N_4 duo to the delocalized big π bonds resulting in low photogenerated electrons and holes recombination. These findings indicate that carbon self-doping is an effective strategy for advancing the g-C_3N_4 materials with high photocatalytic performance. The decreased the photodegradation ability of 8M-CF (over carbon doping) can be ascribed to the facts that the decreased S_{BET} surface lessens the active sites and the near-spherical particles enhances the distance of the photoexcited electrons and holes moving from the inner to surface of the photocatalysts, compared with that of nanosheets structures.

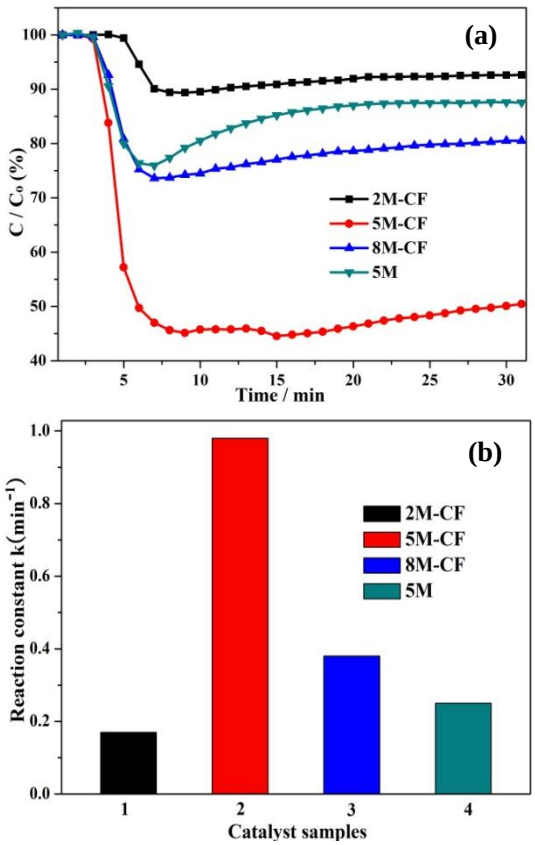

Fig. 10 Photocatalytic activities (a) and apparent rate constants (b) of 2M-CF, 5M-CF, 8M-CF and 5M samples for NO degradation in air under visible-light illumination (λ> 420 nm), (NO concentration: 600 ppb).

In addition, the stability of 5M-CF was further investigated by carrying out the photocatalytic reaction for multiple runs, which was shown in Fig. 11. The photocatalytic performance slightly declines after four repeated runs, which is ascribed to the enrichment of reaction products on the surface of the photocatalysts. However, no obvious deactivation can be observed, demonstrating the promising photocatalytic stability of this catalyst in NO removal.[44-47]

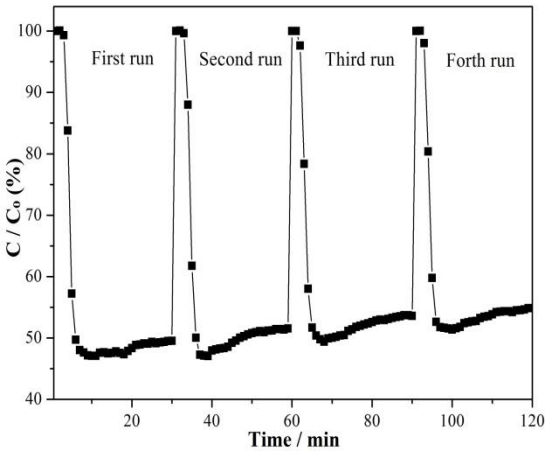

Fig. 11 The stability tests of 5M-CF samples for NO removal under visible light illumination.

5. Conclusion

In summery, (1) we developed an in-situ one-pot strategy to obtain the carbon-rich g-C_3N_4 by using commercially available carbon foam as a soft-temperate. The morphological architectures, intrinsic electronic and band structure of g-C_3N_4 can be fine-tuned via a substitution of lattice nitrogen with carbon.

(2) Proper content of carbon self-doping can significantly enhance the photocatalytic performance on removal of NO in air under visible light.

(3) The conspicuously improved photocatalytic capability is assigned to the co-contributions of the improved S_{BET} surface area, the accelerated electrical conductivity, and the retarded photogenerated electron-holes recombination owing to the formation of delocalized big π bonds. The optimised C-doped g-C_3N_4 photocatalysts also showed good photocatalytic stability. This work could provide new perspectives in design and synthesis of self-doped photocatalyst for enhanced performance.

Acknowledgement

This research is financially supported by the National Natural Science Foundation of China (51478070, 51108487), and the Science and Technology Project from Chongqing Education Commission (KJ1400617).

Notes and references

[a] *Chongqing Key Laboratory of Catalysis and Functional Organic Molecules, College of Environmental and Biological Engineering, Chongqing Technology and Business University, Chongqing, 400067, China.*

[b] *College of Materials Science and Engineering, Chongqing University, Chongqing 400044, P. R. China.*

[c] *National Key Laboratory of Fundamental Science of Micro/Nano-Devices and System Technology, Chongqing University, Chongqing, 400044, P.R. China*

[d] *Department of Chemical and Biomolecular Engineering, Nanyang Technological University, Singapore 639793, Singapore*

*To whom correspondence should be addressed.
E-mail: dfctbu@126.com (Fan Dong), zhangyuxin@cqu.edu.cn (Yuxin Zhang).

1 X.C. Wang, K. Maeda, A. Thomas, K. Takanabe, G. Xin, J. M. Carlsson, K. Domen and M.Antonietti, *Nat. Mater*., 2009, **8**, 76.
2 G. Liu, P. Niu, C. H. Sun, S. C. Smith, Z. G. Chen, G. Q. Lu and H. M. Cheng, *J. Am. Chem. Soc*., 2010, **132**, 11642.
3 R. Asahi, T. Morikawa, T. Ohwaki, K. Aoki and Y. Taga, *Science*, 2001, **293**, 269.
4 Y.P. Bi, S.X. Ouyang, N.T. Umezawa, J.Y. Cao, and J.H. Ye, *J. Am. Chem. Soc*., 2011, **133**, 6490.
5 L.W. Zhang and Y.F. Zhu, *Catal. Sci. Technol.*, 2012, **2**, 694.
6 S.M. Sun and W.Z. Wang, *RSC Adv*.,2014, **4**, 47136.
7 G.P. Dong, Y.H. Zhang, Q.W. Pan and J.R. Qiu, *J.Photoch. Photobiolo. C*.,2014, **20**, 33.
8 J.J.Zhu, P.Xiao, H.L.Li and S.A.C. Carabineiro, *ACS Appl. Mater. Interfaces*, 2014, **6**, 16449.
9 J.S. Zhang, B.Wang and X.C. Wang, *Progress in Chemistry*, 2014, **26**,19.
10 Y.L.Tian, B.B. Chang, Z.C. Yang, B.C. Zhou, F.N. Xi and X.P. Dong, *RSC Adv*., 2014, **4**, 4187.
11 Y.Y. Bu and Z.Y. Chen, *RSC Adv*., 2014, **4**, 45397.
12 Y.G. Li, X.L. Wei, H.J. Li, R.R.Wang, J. Feng, H. Yun and A.N. Zhou, *RSC Adv*., 2014, **0**, 1.
13 X.H. Li, X.C. Wang, and M. Antonietti, *ACS Catal*., 2012, **2**, 2082.
14 Z.W. Zhao, Y.J. Sun and F. Dong, *Nanoscale*, 2015, **7**, 15.
15 F. Dong, Z.W. Zhao, T. Xiong, Z.L. Ni, W.D. Zhang, Y.J. Sun and W.K. Ho, *ACS Appl. Mater. Interfaces*., 2013, **5**, 11392.
16 G. Liu, P. Niu, L.C. Yin, and H.M. Cheng, *J. Am. Chem. Soc*., 2012, **134**, 9070.
17 Z.R. Shen, Z.F. Hu, W.J. Wang, S.F. Lee, D. K. L. Chan, Y.C. Li, T. Gu and J. C. Yu, *Nanoscale*, 2014, **6**, 14163.
18 N. Tian, H. Huang, Y. He, Y. Guo and Y. Zhang, *RSC Adv.*, 2014, **4**, 42716..
19 Y. A. Attia, D. Buceta, C. Blanco-Varela, M. B. Mohamed, G. Barone, and M. A. Ló pez-Quintela, *J. Am. Chem. Soc.*, 2014, **136**, 1182.
20 Y. Di, X.C. Wang, A. Thomas and M. Antonietti, *ChemCatChem*, 2010, **2**, 834.
21 X.H. Li, X.C. Wang and M. Antonietti, *Chem. Sci*., 2012, **3**, 2170.
22 Y.F. Zhang, F. Mao, H.J. Yan, K.W. Liu, H.M. Cao, J.G. Wu and D.Q. Xiao, *J. Mater. Chem. A*, 2015, **3**,109.
23 L. Ge, C.C. Han, J. Liu, Y.F. Li, *Appl. Catal.A: Gen.*, 2011, **409–410**, 215.
24 F. Dong, T. Xiong, Y. J. Sun, Z. W. Zhao, Y. Zhou, X. Feng and Z. B. Wu, *Chem. Commun*. 2014, **50**, 10386.
25 F. Dong, Q.Y. Li, Y.J. Sun and W.K. Ho, *ACS Catal*. 2014, **4**, 4341.
26 S. Paria and O. Reiser, *ChemCatChem*., 2014, **6**, 2477.
27 G. H. Dong and L. Z. Zhang, *J. Mater. Chem.*, 2012, **22**, 1160.
28 S. C. Yan, Z. S. Li and Z. G. Zou, *Langmuir*, 2010, **26**, 3894.
29 G.H. Dong, K. Zhao and L.Z. Zhang, *Chem. Commun.*, 2012, **48**, 6178.
30 F. Zuo, L. Wang, T. Wu, Z. Y. Zhang, D. Borchardt and P. Y. Feng, *J. Am. Chem. Soc.*, 2010, **132**, 11856.
31 K. Xie, N. T. Umezawa, N. Zhang, P. P. Reunchan, Y. J. Zhang and J. H. Ye, *Energy Environ. Sci.*, 2011, **4**, 4211.
32 J.Q. Wang, S.Y. Su, B. Liu, M.H. Cao and C.W. Hu, *Chem. Commun.*,2013, **49**, 7830.
33 J. Jiang, L.Z. Zhang, H. Li, W.W. He and J.J. Yin, *Nanoscale*, 2013, **5**, 10573.
34 Q.J. Xiang, J.G. Yu, W.G. Wang and M. Jaroniec, *Chem. Commun.*, 2011, **47**, 6906.
35 P. Zhang, X.H. Li, C.L. Shao and Y.C. Liu, *RSC Adv.*, 2015, **5**, 15621.
36. F. Dong, Z.Y. Wang, Y.J. Sun, W.K. Ho and H.D. Zhang, *J. Colloid Interface Sci*., 2013, **401**, 70.
37. J.H. Liu, T.K. Zhang, Z.C. Wang, G.H. Dawson and W. Chen *J. Mater. Chem*. 2011, **21**, 14398.
38 A. Iraqi, J. A. Crayston and J. C. Walton, *J. Mater. Chem.*, 1998, **8**, 31.
39 W. D. Zhang, Q. Zhang and F. Dong, *Ind. Eng. Chem. Res.*, 2013, **52**, 6740.
40 F. Dong, Y.H. Li, W.K. Ho, H.D. Zhang, M. Fu and Z.B. Wu, *Chin. Sci. Bull.*, 2014, **59**, 688.
41 F. Dong, S.C. Lee, Z.B. Wu, Y. Huang, M. Fu, W.K. Ho, S.C. Zou and B. Wang, *J. Hazard. Mater*. 2011, **195**, 346.
42 F. Dong, M.Y. Ou, Y.K. Jiang, S. Guo and Z.B. Wu, *Ind. Eng. Chem. Res*., 2014, **53**, 2318.
43 S. Zheng, W.J. Jiang, M.Rashid, Y.Cai, D. D. Dionysiou and K. E. O'Shea, *Molecules*, 2015, **20**, 2622.
44 F. Dong, Z. Wang, Y. Li, W. Ho, S. Lee, *Environ. Sci. Technol.*, 2014, **48**, 10345.
45 T. Xiong, H. Huang, Y. Sun and F. Dong, *J. Mater. Chem. A*, 2015, **3**, 6118.
46 Z. Wang, W. Guan, Y. Sun and F. Dong, Y. Zhou and W. K. Ho, *Nanoscale*, 2015, **7**, 2471.
47 F. Dong, H. T. Liu, W. K. Ho, M. Fu and Z. B. Wu, *Chem. Eng. J.*, 2013, **214**, 198.